

Date of publication xxxx 00, 0000, date of current version xxxx 00, 0000.

Digital Object Identifier 10.1109/ACCESS.2024.Doi Number

Evaluation of the Performance of new type of Segmented Stator Permanent Magnet Synchronous Motor

Hairul Faizi Hairulnizam¹, Norhisam Misron^{1, 2, 3}, Nur Amira Ibrahim¹, Hafiz Rashidi Ramli¹, Chockalingam Aravind Vaithilingam^{4, 5}

¹Faculty of Engineering, Universiti Putra Malaysia, Serdang, Selangor 43400, Malaysia

Corresponding author: Norhisam Misron (norhisam@upm.edu.my) and Hairul Faizi Hairulnizam (GS67769@student.upm.edu.my)

This work was supported by Universiti Putra Malaysia (UPM).

ABSTRACT The paper presents the evaluation study to enhance the design of the motor's permanent magnet (PM), with the goal of increasing the performance of the segmented stator Permanent Magnet Synchronous Motor (PMSM). The rotor is externally mounted and embedded permanent magnet placed into the groove. By adjusting the width, tip angle, ratio dimension and skew angle of the PMs optimize the magnetic flux flow inside the motor thereby improving performance of the motor under considerations. Finite Element Method (FEM) is used to evaluate for optimizing the parameters to reach the maximum torque through parametric optimization. The numerical results are compared in terms of static torque, cogging torque, iron losses, torque-to-detent torque ratio, and torque constant parameter variations of the models. The findings with optimized flux flow evolve a new type of outer rotor embedded PMSM structure that is fabricated and tested for practical adoption for static and dynamic characteristics. The proposed new type of segmented rotor exhibits low cogging torque with torque ratio of 62 against the conventional structure with value of 14. The proposed model is fabricated and evaluated for its performance against the numerical results and are in close agreement.

INDEX TERMS Torque Ratio, PMSM, Cogging torque, Outer Rotor, Segmented Stator, Finite Element Analysis

I. INTRODUCTION

Permanent magnet (PM) motors are becoming increasingly popular due to their multiple benefits, including high power, torque density, efficiency, low maintenance, and dependability. PM motors are well-suited for application in a wide range of industries [1], [2]. The advancement in PM materials lead to the development of high-performance permanent magnet synchronous motors (PMSM) [3]. PMSM efficiencies range from 92% to 97%, making them suitable for electric vehicle applications [4]. The exceptional torque-speed characteristics render PMSMs optimal for electric vehicles, making them a favoured alternative to early DC motor drives [5]

To improve the motor's efficiency, specialists prioritize optimizing the PMSM structure, which includes both the PM and iron components such as the rotor and stator. The consequent pole PM rotor is a technique developed by researchers to reduce dependency on PM rotors. This arrangement reduces expenses by 30% by lowering the volume of PM [6], [7], [8]. While the use of cheap PM materials, such as ferrite, is a promising technique to cut costs, the restricted torque density provides a barrier [9]. Furthermore, the motor's rotary component may be positioned either inside or outside, giving the motor different capabilities. The inner rotor architecture is often used because it ensures that the amplitude of the airgap flux density nearly matches the magnetic flux density of the PM. This allows for operating at a greater range of velocities,

²Institute of Nanoscience and Nanotechnology, Universiti Putra Malaysia, Serdang, Selangor 43400, Malaysia

³Institute of Plantation Studies, Universiti Putra Malaysia, Serdang, Selangor 43400, Malaysia

⁴Clean Technology Impact Lab, Taylor's University, Subang Jaya, Selangor 47500, Malaysia

⁵Adjunct Professor, Vel tech Rangarajan Dr. Sanguthala R and D Institute of Science and Technology, Chennai, Tamilnadu 600092, India



ultimately leading to an effective ability to lower flow [10]. It is worth mentioning that the outer rotor has a net mass that is 15% lower than the inner rotor's, resulting in reduced transmission losses [11].

The outer rotor PM machine may have a high torque density, but it requires a substantial amount of rare-earth PM material [12]. The rising cost of rare-earth PM is greatly impeding PMSM development, resulting in greater PMSM production costs [13] Given this knowledge, the study referenced in reference [14] investigated numerous magnetic materials to find effective ways to reduce or eliminate the need for rare-earth in PM motors. The study's findings show that samarium, while categorised as a rare-earth magnet, performs best at lower speeds. When fully loaded, it achieves an amazing 92.5% efficiency with AlNiCo full-load efficiency, at 75.7%.

A PM motor with a segmented stator design has the potential to cut costs, enhance flexibility, and reduce winding [3] [15][16] Segmented structures are extensively utilised in switched reluctance motors (SRM) due to its ability to attain a 93.3% rise in efficiency relative to comparable motors and to enhance output torque by 63.91%, with average torque rising by as much as 60% [17][18][19]. According to prior research, the segmented stator outperformed the conventional salient pole stator design, demonstrating a 79.97% enhancement in average torque, a 90.89% improvement in maximum torque, and a 3.02% reduction in cogging torque. The results indicate that the segmented stator exhibits superior efficiency compared to the salient pole stator [20]. Furthermore, the use of a segmented stator improves the motor's output torque, with increased torque with low cogging torque, a feature that is critical in applications including electric vehicle and energy generations.

With the motivation from the previous study, this work seeks to evaluate the performance of segmented stator design that works in tandem with an integrated permanent magnet synchronous motor with split teeth on the outer rotor. The segmented stator motor is modelled in two dimensions with the finite element method and the motor characteristics with parametric optimization to derive the improved design. Different variations of the motor are compared for its static torque produced, cogging torque, their ratios, the iron losses, and torque constant. Besides, the simulated results are compared to the experimental results in terms of torque and speed for performance evaluation of such machines for practical applications.

II. DESIGN CONFIGURATION

A. SEGMENTED CONFIGURATION

FIGURE 1 illustrates a segmented stator with divided teeth and an outer rotor housing a permanent magnet synchronous motor. The rotor, the motor's rotating element, comprises thirty-two poles, each embedded with permanent magnets within the teeth. The magnetization direction of each successive permanent magnet is reversed relative to its predecessor. These PMs aim to enhance torque and power densities by augmenting the magnetic flux density across the air gap. The motor is configured with three phases, each featuring two concentrated windings. Additionally, a proposed segmented stator design incorporates a half-pitch magnet gap between phases. The segmented stator architecture of the motor delivers superior performance, particularly in terms of generated torque, cogging torque, and minimizing losses. **TABLE 1** provides the critical preliminary specifications and dimensions of the proposed motor.

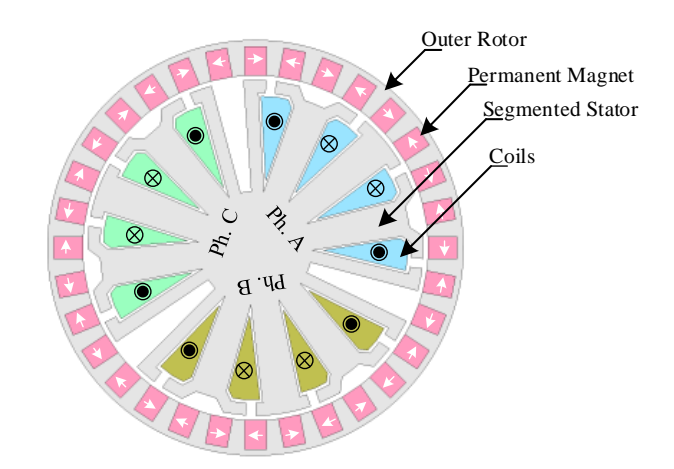


FIGURE 1 Structure of the segmented stator motor

TABLE I
PRELIMINARY MOTOR DIMENSIONS AND PARAMETERS

Parameters	Values	
Number of phases	3	
Stator outer radius (mm)	13.63	
Rotor inner radius (mm)	14.13	
Rotor outer radius (mm)	17.0	
PMs width/length (mm)	1.8/2.4	
Total volume of PM (mm ³)	8292.4	
Total volume of rotor (mm ³)	6486o	
Total volume of stator (mm3)	16141.7	
Number of magnets	32	
Stack length (mm)	45	
Air-gap length (mm)	0.5	
Number of turns per pole	18	
Coil diameter (mm)	0.6	
Magnet material	NdFeB	
Stator and rotor material	50H800	
Rotational speed (rpm)	1000	



B. MAGNETIC FLUX ANALYSIS

FIGURE 2 depicts the projected flow of magnetic lines used to demonstrate the operation of the motor. When just the coil is energized, the magnetic field it creates travels through the air gaps, through the stator and rotor yokes, and ends at the pole's excited phase windings. When the windings are not connected to create a complete circuit, no electric current passes through them. When the armature winding is turned on, the magnetic flux from the permanent magnet penetrates the gaps between the rotor and stator due to the magnetic field's force. The stator's centre pole lets magnetic flux pass through the air gaps throughout all phases of operation. When flux flows through the centre stator pole of the motor, it slows down. Shorter flux flow decreases the motor's losses. As a result, the presence of permanent magnets in the rotor contributes significantly to the motor's air gap flux density.

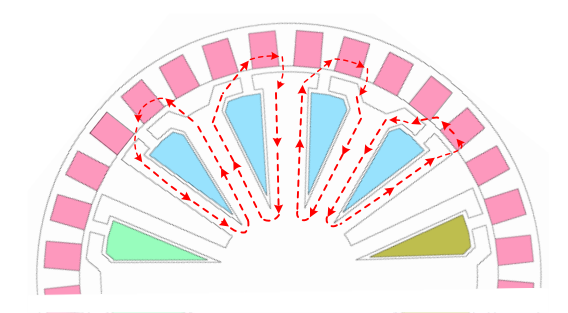


FIGURE 2 Flux flow of the segmented stator motor

C. DEVELOPED TORQUE INSIDE THE MOTOR

The torque generated in segmented stator and salient pole designs varies due to their distinct topologies. To examine the discrepancies, we can utilize the generic torque Equation (1).

$$F = -\frac{\partial W}{\partial \theta} \tag{1}$$

The energy (W) is typically stored in a magnetic field, with θ representing the position angle. Equation (2) represents the amount of work performed.

$$W = \frac{1}{2}\lambda i = \frac{1}{2}Ni\Phi = \frac{1}{2}Li^2$$
 (2)

The expression for W can alternatively be described in terms of flux linkage (λ), current (i), number of turns (N), magnetic flux (Φ), and inductance (L), as shown in Equation (3).

$$\Phi = NiP = BA \tag{3}$$

The permeance (P) is defined as the reciprocal of resistance (R). Therefore, by utilizing equations (1), (2), and (3), the formula for thrust (F) is as shown in Equation (4).

$$F = -\frac{1}{2}(Ni)^2 \frac{\partial P}{\partial \theta} \tag{4}$$

The equation is further expanded as in Equation (5).

$$NI = N_c I_c + N_m I_m \tag{5}$$

The total magneto motive force (MMF), NI generated in the motor is comprised of the magnet MMF, $N_m I_m$ produced in the rotor containing with magnets, and the coil MMF, $N_c I_c$ generated by the stator wound with the coil winding. When evaluating the values of $N_c I_c$ and $N_m I_m$ the Equation (6) is derived.

$$F = -\frac{1}{2} (N_c I_c + N_m I_m)^2 \frac{\partial P}{\partial \theta}$$

$$F = \frac{1}{2} (N_m I_m)^2 \frac{\partial P}{\partial \theta} - (R_c I_c) \cdot (N_m I_m) \frac{\partial P}{\partial \theta} - \frac{1}{2} (N_c I_c)^2 \frac{\partial P}{\partial \theta}$$
 (6)

The cogging torque, which reduces the motor's overall force production, is indicated by the first term in Equation (6). The final section of the equation depicts the relationship between coil flux and permanent magnet flux. The last component of the equation estimates the total force, considering the reluctance torque generated by the motor. It is seen from Equation (6), the torque output of the comparison motor is governed by parameters such as cogging torque, the degree of interaction between coil flux and PM flux, and reluctance torque [21]. The proposed motor is especially designed to conform to equation (6), which attempts to optimize the interplay between coil flux and PM flux and lower resistance torque, while simultaneously reducing torque. Converging the Equation (4) in Equation (6), the fundamental equations for the cogging torque, thrust, and resistance torque is derived as in Equation (7) the required force (F).

$$F = \frac{B_g^2 A}{2\mu_0} - NiBl - \frac{1}{2} \frac{\partial L}{\partial \theta} i^2$$
 (7)

D. FINITE ELEMENT ANALYSIS

Finite Element Analysis (FEA) is used to identify the basic magnetic characteristics of the motor under consideration. Examine the electromagnetic characteristics of the suggested design by using the 2-D finite element technique (FEM). This study makes use of the JMAG software suite developed by JSOL Corporation. The two-dimensional finite element technique (FEM) is chosen over the three-dimensional FEM because it allows for faster simulation assessment and is more accurate. The electromagnetic properties using Maxwell is as shown in Equation (8).



$$\Omega: \frac{\partial}{\partial x} \left(v \frac{\partial y}{\partial x} \right) + \frac{\partial}{\partial y} \left(v \frac{\partial y}{\partial y} \right) \tag{8}$$

$$= -J - v \left(\frac{\partial Bry}{\partial x} - \frac{\partial Brx}{\partial y} \right) + \sigma \frac{\partial A}{\partial t}$$

The computational field solution zone is denoted by Ω , the magnetic vector potential by A, the current density by J, v represents reluctivity, σ denotes electrical conductivity, and Bry and Brx represent the components of remanent flux density.

FIGURE 3 illustrates the magnetic density of the segmented stator when the winding is energised at 10A. The motor utilised 50H800 steel for both the rotor and stator components. This material has a knee point saturation at 1.5T. The segmented stator of the motor is not saturated, indicating a well-designed stator.

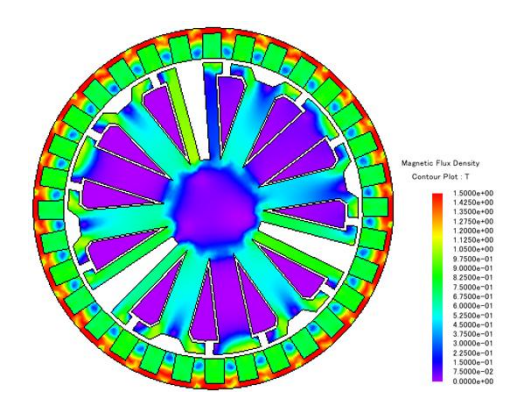


FIGURE 3 Magnetic Density of the segmented stator

III. DESIGN CONSIDERATION AND EVALUATION

This study aims to investigate the influence of the PM magnetic potential on torque generation within the machine. Further exploration is required to determine the optimal specifications and dimensions of the PM to be integrated into the motor. The PM is positioned within the rotor slot, thereby rotating in conjunction with the rotor. Incorporating PMs reduces the amount of iron necessary for rotor construction, which could potentially compromise the motor's performance. Four critical dimensional parameters are examined: the magnet's width (W_{PM}), tip angle of PM ($T_{\Theta PM}$), ratio of PM (R_{PM}) and angle (Θ_{PM}), as depicted in FIGURE 4. These parameters are analysed for evaluation purposes. FEA is employed to ascertain the optimal values for WPM, HPM and OPM, based on initial motor structure data: a stator outer diameter of 27.62 mm, a rotor outer diameter of 34 mm, an air gap of 0.5 mm, and a stack length of 45 mm. The evaluation outcomes are detailed in TABLE 2. To facilitate comprehension, specific

designations are assigned to various model variations: width variations (A, B, C), tip angle variation (K, L, M) ratio variations (P, Q, R) and skew angle variations (X, Y, Z).

A. WIDTH VARIATION OF THE MAGNET (WPM)

One of the key parameters examined in this study is WPM as illustrated in Figure 4(a). The base model features a PM with dimensions of 2.4 mm in width and 2.4 mm in height. The geometric dimensions of the PMs play a pivotal role in shaping the motor's magnetic performance and overall efficiency. This study aims to determine whether increasing the PM width to the maximum allowable limit before the magnets physically interfere with each other enhances the motor's performance. Identifying the optimal magnet width is essential for enhancing critical performance metrics, including iron losses, torque generation, and cogging torque. For our analysis, we established a series of width variations while keeping the height and length parameters fixed at 2.4 mm and 45 mm, respectively. Modifying the magnet's width impacts the rotor's pole arc, thereby influencing the amount of iron utilized in the rotor.

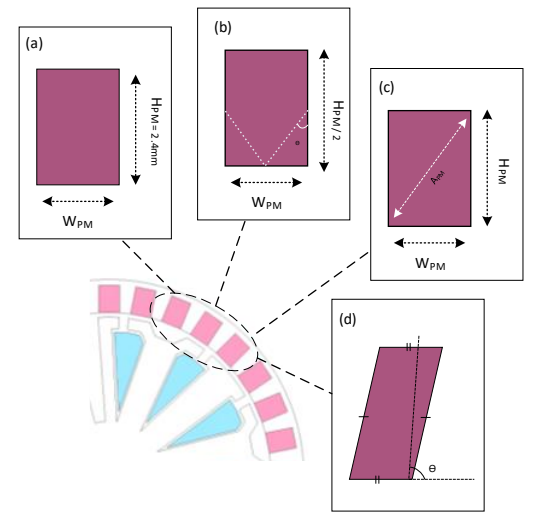


FIGURE 4 Optimized parameter of the motor structure by varying (a) width (b) tip angle (c) ratio (d) skew angle.

B. TIP ANGLE VARIATION OF PM (TOPM)

Subsequently, we assess the motor's performance when the PM are tapered and oriented at specific angles, as depicted in Figure 4(b). The adoption of tapered PMs could potentially decrease the quantity of magnet material needed, thereby reducing manufacturing costs. This study aims to evaluate and analyze the impact of tapered permanent magnets on the motor's output performance compared to the conventional rectangular magnets currently in use. In this configuration, the magnet's height is reduced to half of H_{PM} which is the origin when it tapered, while the width is fixed at 1.8 mm.



TABLE 2
MAGNET EVALUATION WITH DIMENSION AND CONSTANT VALUES

Magnet Variation	Model	Dimension (W x H)	Constant
Width Variation	А	1.8mm x 2.4mm	
	В	2.4mm x 2.4mm	$H_{PM} = 2.4$ mm
	С	2.7mm x 2.4mm	
Tip Angle Variation	K (15°)	15°	
	L (30°)	30°	W _{PM} = 2.4mm
	M (45°)	45°	$H_{PM}/2 = 1.2$ mm
Ratio Variation	Р	1.543mm x 2.8mm	
	Q	2.7mm x 1.6mm	$V_{PM} = 216 \text{mm}^3$
	R	2.08mm x 2.08mm	
Skew Angle Variation	X (50°)	1.98mm x 2.85mm	
	Y (70°)	1.86mm x 2.47mm	$V_{PM} = 216 \text{mm}^3$
	Z (85°)	1.8mm x 2.399mm	

C. RATIO VARIATION WITH SAME VOLUME (RPM)

PMs play a critical role in enhancing machine performance by increasing output generation. In this study, we explore various dimensional ratios of PMs within our proposed motor structure to understand how these ratios influence the motor's behavior. Specifically, we vary the width (W_{PM}) and height (H_{PM}) of the magnets while keeping the stack length (L_{PM}) constant at 45 mm and the magnet volume (V_{PM}) fixed at 216 mm³. This approach allows us to maintain consistency across the experiments with having same volume's constraint while adjusting the aspect ratios of the PMs.

D. SKEW ANGLE VARIATION OF THE MAGNET (Θ_{PM})

In our final study, we explore the impact of skewing the PMs at various angles to assess their effect on motor performance. Starting with a base model where the PMs are positioned at a 90-degree angle, we incrementally adjust the skew angle down to 50 degrees. This allows us to determine whether skewing enhances motor performance or if the original perpendicular alignment is optimal. As skewing alters the PM shape from a rectangular to a parallelogram, maintaining a consistent volume across all models is essential for a fair comparison. To ensure the volume of PM remain constant, we use (9) to calculate the cross-section area of parallelogram.

$$A_{paralellogram} = a \times b \times sin(\theta) \tag{9}$$

Where the a and b represent the length of sides for the shape and θ is the skew angle of magnet. Furthermore, we enforce another constraint in this study in which the distance between any edge of PM when skewed and the outer diameter of rotor must remain constant across all models.

2

IV. NUMERICAL ANALYSIS FROM FEA

A. GENERATED TORQUE

FIGURE 5(a) elucidates the output torque generated for each model in width variation when injected with 12.5A current source. This analysis stands alone and is not compared to other studies due to variations in PM volumes, which render direct comparisons unsuitable. Upon reviewing the graph, Model B delivers output torque that exceeds Model A by 4.18% and Model C by 10.39%. Surprisingly, Model A, despite having the smallest PM volume—with a width of just 1.8 mm, 0.9 mm less than Model C—produces 6.48% more output torque than the largest model. Furthermore, noticeable ripples in the torque profiles of Models B and C indicate elevated cogging torque in these motors. This finding suggests that increased PM volume does not consistently correlate with enhanced motor performance.

Subsequent analysis investigates the impact of varying the magnet's tip angle, set at 15° , 30° , and 45° . **FIGURE 5(b)** presents the torque output for these configurations, demonstrating that the 15° angle yields a torque 4.36% higher than the baseline model, which features a 0° tip angle. Nevertheless, the 0° model surpasses Models L and M, achieving torque outputs that are 16.54% and 151.31% greater, respectively. The diminished performance of Models L and M can be attributed to a substantial reduction in magnet volume relative to the 0° model.

FIGURE 5(c) evaluates motor performance when the dimensional ratio of the PM is modified. In this study, the PM volume is constrained to align with that of the reference model, ensuring the reliability and comparability of the results. The graph indicates that Model A surpasses Model Q and R with 32.94% and 31.99% increment respectively.

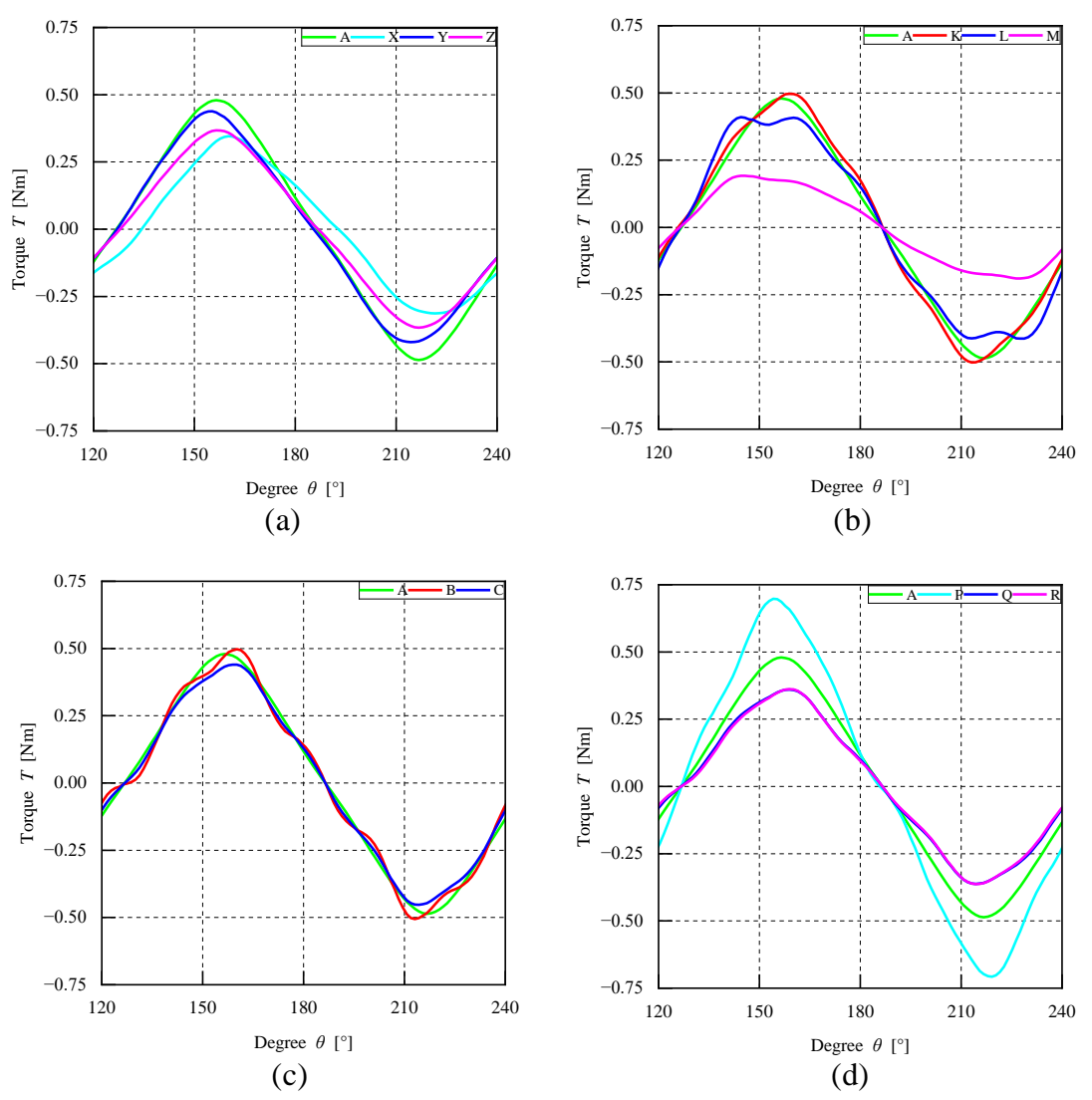


FIGURE 5 Static torque generated when varies (a) width of PM (b) tip angle of PM (c) ratio of PM (d) skew angle

However, Model P distinguished by its elongated and slender magnet design, outmatch Model A by producing 0.698Nm or 44.56% larger torque.

The final study examines torque generation when the PMs are skewed at angles of 50°, 70°, and 85°, relative to the reference model at 90°. Both the PM volume and the distance between the PM and the rotor back iron is held constant, consistent with the base model. **FIGURE 5(d)** shows that deviating from the 90° angle reduces torque output, with decreases of 38.66% for Model X, 10.16% for Model Y, and 25.57% for Model Z.

B. COGGING TORQUE

Cogging torque is an unfavourable output that diminishes motor performance. To ensure that the motor is in an optimal condition, it is imperative to minimize or eliminate entirely the cogging torque. This phenomenon arises from the interaction between the PM's magnetic flux and the

stator teeth, occurring even in the absence of electrical current (zero current) in the coils. Consequently, the coils remain unenergized, yet the presence of permanent magnets induces torque, even under no-load conditions. To evaluate the detent torque generated, the highest values are taken from each model. When examining the interaction between the magnet and ferromagnetic iron at zero current, Model A outperforms both Models B and C. The detent torque, calculated from the peak output value, reveals significant differences. As depicted in FIGURE 6(a), Model B and C generated 476.43% and 272.01% bigger detent torque contrasted to Model A. These substantial differences underscore Model A's ability to provide smoother and more stable operation than its counterparts. The peak cogging torque values further highlight the pronounced disparities between the models. Based on these initial tests, Model A emerges as the most suitable base reference for subsequent evaluation studies.



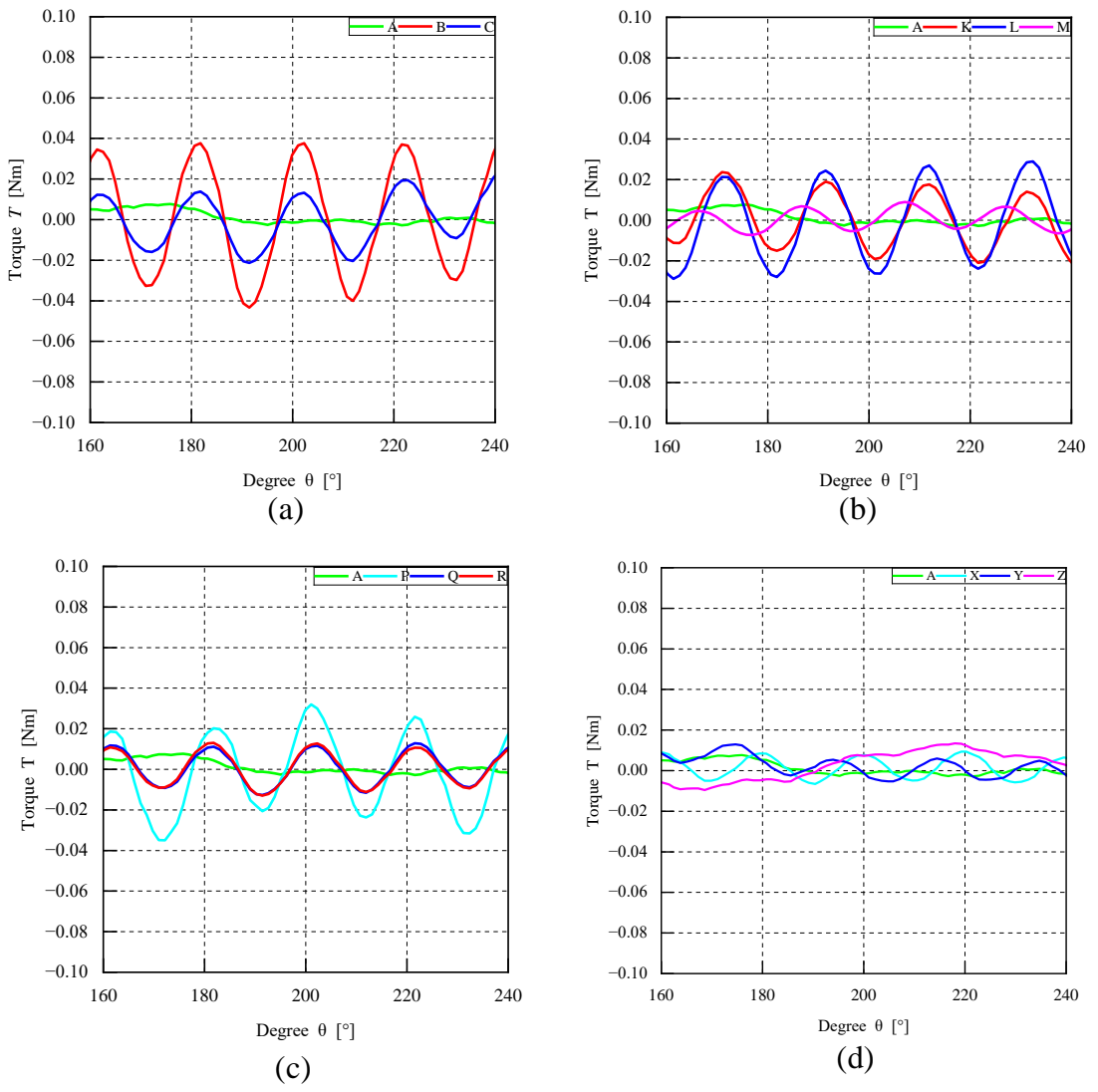


FIGURE 6 Cogging torque generated when varies (a) width of PM (b) tip angle of PM (c) ratio of PM (d) skew angle

This selection is driven by its markedly reduced cogging torque, coupled with only a marginal reduction in static torque output. These attributes position Model A as an ideal starting point for further refinement, effectively balancing smooth operation with efficient torque production. Furthermore, **FIGURE 6(b)**, **(c)** and **(d)** provide additional comparisons of cogging torque across various motor models relative to Model A. In all cases, Model A consistently maintains the lowest cogging torque, reinforcing its superior performance. For instance, in the tip angle variation, Models K, L, and M—despite having smaller PM volumes than the base model-generate cogging torques that are 221.09%, 303.39%, and 16.93% larger than Model A's, respectively. Similarly, in evaluations where the PM volume is held constant, such as those involving ratio dimension and skew angle variations, Model A continues to outperform its peers. Specifically, Models P, Q, R, X, Y, and Z exhibit cogging torques that are 324.09%, 84.11%, 105.08%, 27.60%, 96.88%, and

74.48% larger than Model A's, respectively. These findings affirm Model A's dominance in minimizing cogging torque across diverse design configurations. In essence, the placement of permanent magnets in Model C's motor assembly has been optimized to achieve exceptionally low cogging torque.

C. TORQUE RATIO

To assess the motor's performance quality, a torque/cogging ratio is introduced, which compares the maximum generated torque to the undesirable cogging torque. This ratio is calculated using equation (10), where the ratio is the division of the maximum torque (T_m) by the cogging torque (T_c) .

Torque Ratio (TR) =
$$\frac{T_m}{T_c}$$
 (10)



FIGURE 7 illustrates the torque/cogging ratio across all variations in this study, with Model A achieving the highest ratio among all tested models. Specifically, Model A's torque/cogging ratio surpasses that of Models B, C, K, L, and M by 452.27%, 297.78%, 207.67%, 370.45%, and 193.94%, respectively, resulting in an effective torque 62 times greater than its cogging torque, which highlights its superior performance. This dominance persists in variations where the PM volume remains constant. For instance, in the magnet ratio dimension variations, Model A is shown to be 2.94 times more effective than Model P, 2.45 times better than O and 2.71 times than Model R. Similarly, in the skew angle variations, excluding Model A, Models X, Y, and Z achieve ratios of 35, 28, and 36, respectively—values that are still approximately half of Model A's ratio, further emphasizing its exceptional effectiveness efficiency and across different configurations.

D. IRON LOSSES

FIGURE 8 provides a detailed summary of iron losses across various analysed motor models, significant differences in efficiency due to flux flow dynamics. Model M demonstrates the lowest iron loss at 7.61 W, marking it as the most efficient in managing flux. Conversely, Model P shows the highest iron loss at 25.3 W, with Model C and O closely trailing at approximately 25 W, indicating notable inefficiencies in their designs. Model A produces 16.34W where it ranks sixth out of twelve models. This value reflects a 53.41% increase in losses compared to the highly efficient Model M, yet a 55.03% decrease relative to the least efficient Model P. These findings emphasize the critical impact of flux flow variations on iron losses, highlighting the importance of optimized motor design to reduce energy dissipation and improve overall efficiency.

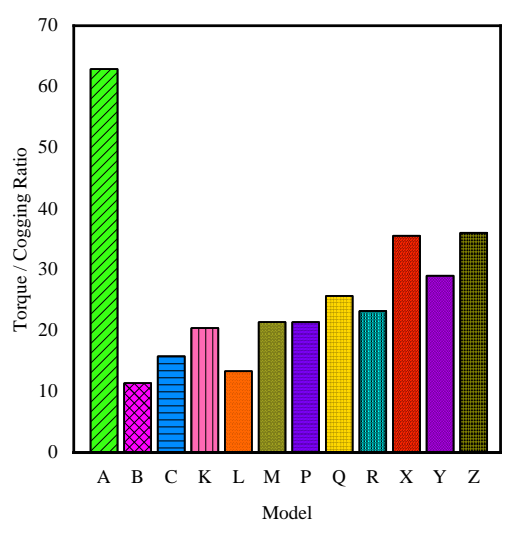


FIGURE 7 Torque cogging ratio for various developed models

2

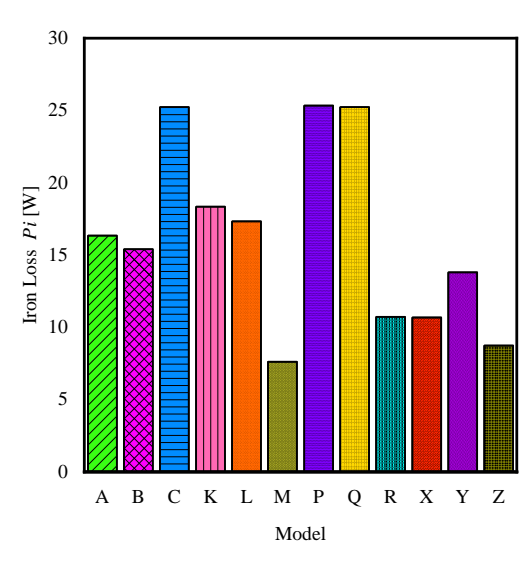


FIGURE 8 Iron losses for various developed models

E. COMPARITIVE ANALYSIS

FIGURE 9(a), (b), (c) and (d) present radar graphs comparing the developed models across key performance metrics: iron losses (Pi), torque/cogging torque ratio (Tm / Tc), maximum torque generated (Tm), cogging torque (Tc), and torque constant (K_T). These radar graphs are organized based on the parameter variations discussed in Section 4 which are width, tip angle, ratio and skew angle.

FIGURE 9(a) and 9(b) focuses on width and tip angle variations. Analysis in **FIGURE 9(a)** reveals that Model B incurs the lowest iron losses, while Model C exhibits the highest. However, when considering the comprehensive set of performance metrics, Model A surpasses Models B and C.

FIGURE 9(b) extends the analysis to angle variations. The results mirror those of the width study, with Model A again displaying a perfect pentagonal shape, signifying well-rounded performance across all evaluated parameters. Model A's radar graph forms a nearly perfect pentagon, indicating balanced excellence with high values for Tm, Tm/Tc, and KT, alongside the lowest Tc and moderate iron losses. Thus, Model A is optimal for applications demanding both high torque and smooth operation.

Since variations (a) and (b) involve models with different magnet volumes, the comparison using the radar graph is not entirely accurate. To address this issue and enable a more meaningful evaluation, the analysis proceeds with an variation approach that constrains the magnet volume to be identical across all models. By standardizing the magnet volume, this method eliminates its effect as a variable, allowing for a clearer and more precise comparison of other design parameters.



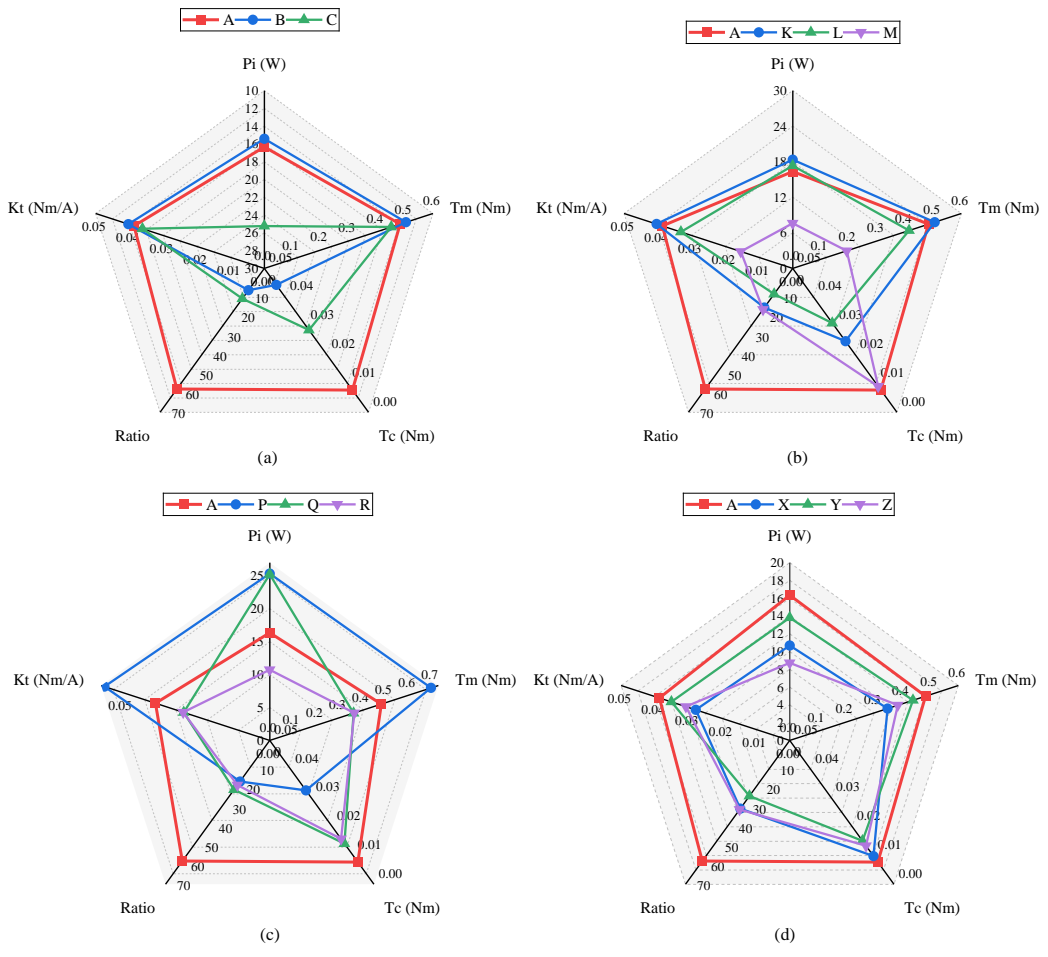


FIGURE 9 Radar graph when varies (a) width of PM (b) tip angle of PM (c) ratio of PM (d) skew angle

FIGURE 9(c) shows that model P has the highest T_m produced and K_T value, but they generate a substantial number of P_i and T_c. Model P is most likely suited for applications requiring a high torque per unit current, although it is less appropriate for high efficiency applications. Model A, on the other hand, has a pentagon structure, suggesting superior and balanced performance based on the data analysed. Model C is ideal for applications requiring smooth operation due to its exceptionally low Tc FIGURE 9(d) presents a radar graph for models where both the magnet volume and the distance between the magnet edges and the iron rotor are held constant. The PM are skewed by specific angles to evaluate their impact on performance. Analysis of the radar graph in FIGURE 9(d) reveals that Model A outperforms the other models when the objective is to design a balanced motor. Although the other models also exhibit nearly pentagonal shapes—indicating a degree of balanced performance—their smaller sizes suggest lower overall performance levels. By comparing FIGURE 9(c) and (d) it depicts that Model A is the optimal choice for a motor that delivers high torque production alongside the lowest detent torque, ensuring both power and smooth operation.

V. EXPERIMENTAL AND COMPARISON RESULT

A. FABRICATION AND EXPERIMENTAL SETUP

Model A selected based on its promising performance during the design phase, was subsequently fabricated for experimental validation. FIGURE 10(a) illustrates the segmented stator, while **FIGURE 10(b)** shows the rotor with embedded permanent magnets. The permanent magnets, made of neodymium iron boron, are integrated into the rotor, which, along with the stator, is constructed from 50H800 steel. The stator windings consist of 18 turns of 0.5 mm diameter wire. The motor features a stack length of 45 mm and an air gap of 0.5 mm between the stator and rotor. FIGURE 10(c) illustrates the fully assembled segmented prepared for experimental evaluation. comprehensive experimental setup, as shown in FIGURE 11 includes a sensor-less driver board for motor control, a tachometer for speed measurement, a torque meter to quantify output torque, and a DC power supply. This setup enables detailed characterization of the motor's torque-speed performance, validating the design through empirical data and facilitating comparison with simulation results.









FIGURE 10 Fabricated component (a) Assembled motor (b) Outer Rotor and Magnet (c) segmented stator

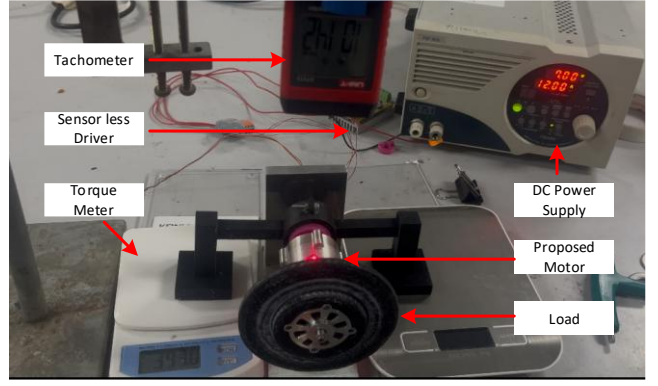


FIGURE 11 The experimental setup for segmented stator motor

B. STATIC TORQUE

FIGURE 12 presents the static torque characteristics of the system under three distinct current levels 1 A, 3 A, and 5 A—comparing experimental results (depicted by solid lines) with simulation outcomes (represented by dashed lines). The torque displays a sinusoidal pattern across an angular range of 0° to 21°. Notably, the experimental and simulation results exhibit strong agreement in terms of shape and periodicity. For example, when the motor is energized with current, the torque profiles generated from both experimental and simulation approaches are closely aligned. Nevertheless, minor discrepancies are observed in the experimental data, likely attributable to measurement noise, which introduces ripples into the torque curves.

At a current of 1 A, the difference between experimental and simulation results is approximately 6.21%. This deviation decreases to 4.58% when the current is increased to 3 A, where the sinusoidal waveform exhibits minimal ripples and closely mirrors the simulated profile. At 5 A, however, the divergence becomes more pronounced, with a peak difference of 8.42%, though the periodicity of the waveform remains intact. This

increased deviation may stem from unmodeled factors such as friction and magnetic saturation, which are not fully captured in the simulation. Overall, the experimental findings substantiate the validity of the simulation results obtained using finite element analysis (FEA) software, reinforcing the reliability of the computational model despite these minor inconsistencies.

C. TORQUE CONSTANT

The torque constant represents a linear relationship between torque and current, quantifying the torque generated per unit of current. As illustrated in FIGURE 13, both experimental and simulated torque constants exhibit a near-linear trend. Analysis of the graph reveals that the experimental torque increases from 0 A to 5 A, reaching approximately 0.176 Nm at 5 A, whereas the simulation predicts a value 7.62% higher. This reflects a strong correspondence between the simulated and experimental results, with only a marginal discrepancy. The torque constant can be determined by calculating the slope of the linear trendline. The percentage difference between the two slopes is approximately 7%. The close alignment between the experimental and simulated outcomes substantiates the validity of the model under linear operating conditions; however, the slight divergence observed at higher currents indicates potential areas for future refinement.

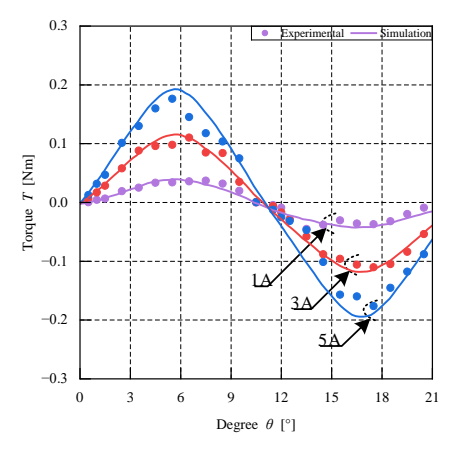


FIGURE 12 Static torque comparison between simulation and experimental

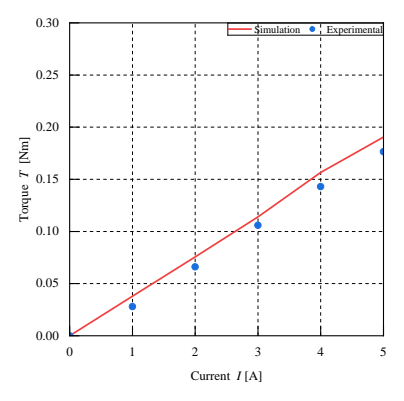


FIGURE 13 Torque constant between simulation and experimental



D. SPEED TORQUE CHARACTERISTICS

FIGURE 14 illustrates the torque-speed characteristics of the fabricated motor, providing insight into its dynamic response and validating the effectiveness of the proposed design. The motor was experimentally tested under two voltage input conditions: 7 V and 10 V, with the simulation assuming an ideal maximum operating speed of 2000 rpm. However, due to mechanical inherent in the constructed prototype, the actual maximum speed achieved during testing was limited to 1250 rpm A comparative analysis between the experimental results and the simulation data reveals a generally close agreement, affirming the accuracy of the design and modelling assumptions. Under an injection voltage of 7 V, the torque-speed curve from the experimental results exhibits a percentage deviation of approximately 8% at 500 rpm when compared to the simulated values. However, as the input voltage was increased to 10 V, the deviation between experimental and simulated results became more pronounced, reaching 29% at 500 rpm. This increase in discrepancy is likely attributed to several nonideal factors present during experimental testing which become more significant at higher operating conditions.

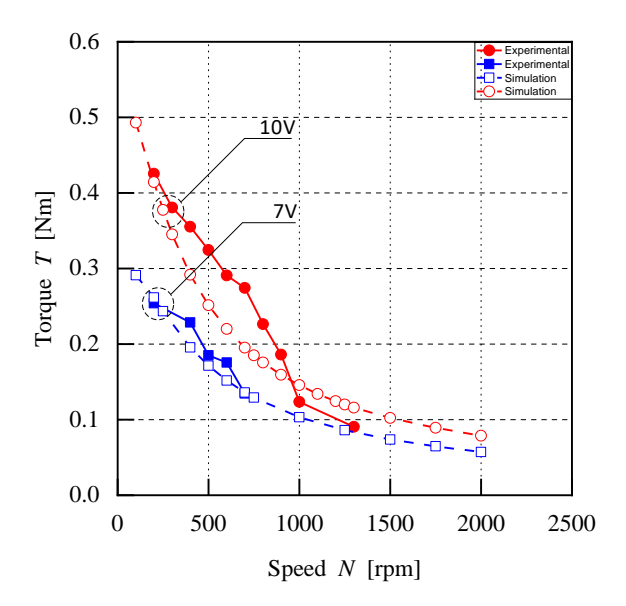


FIGURE 14 Torque speed characteristics of the simulated and fabricated motor

E. COMPARISON WITH CONVENTIONAL STRUCTURE

FIGURE 15 provides a performance comparison of the two motors when operated with a DC current source. The analysis reveals that the proposed segmented stator structure achieves a torque output that is 135.79% higher than that of the conventional salient pole design. Furthermore, the segmented stator reduces detent torque by 45.22% relative to

8

the conventional structure, indicating a significant improvement in operational smoothness.

FIGURE 16 a comparative illustration of the proposed segmented stator structure alongside the conventional salient pole stator design. Both motor configurations are engineered with identical parameters, including the number of magnets, motor diameter, air gap size and stator diameter, ensuring a consistent basis for evaluation. Additional insights are derived in

Further quantitative performance metrics are consolidated in **TABLE 3**, offering a detailed comparative overview of key parameters such as torque, cogging torque, ratio, torque constant and iron losses. The data strongly affirm the superiority of the proposed segmented stator motor, not only in terms of torque enhancement but also in operational smoothness, thus validating the design as a viable and effective alternative to traditional motor configurations.

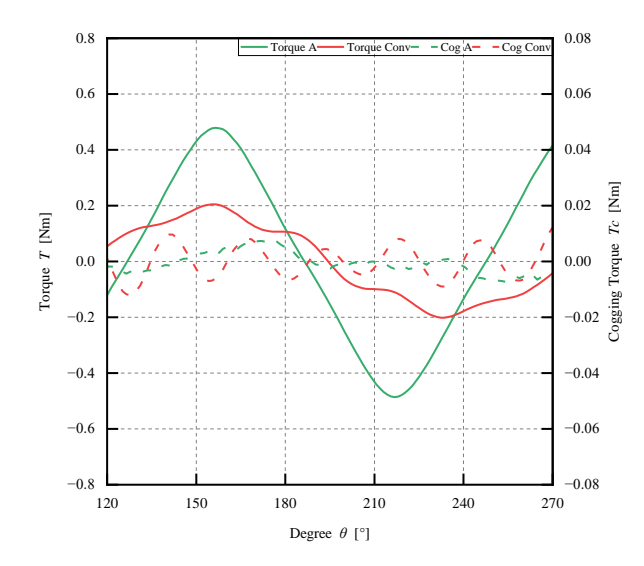
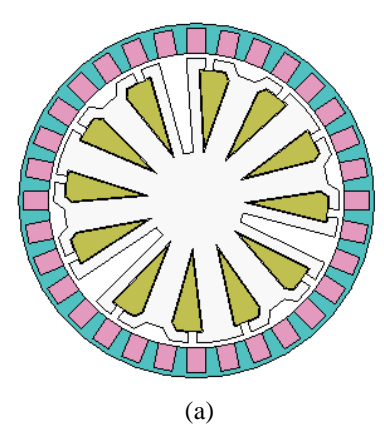


FIGURE 15 Torque and detent torque between Model A and Conventional

TABLE 3
PRELIMINARY MOTOR DIMENSIONS AND PARAMETERS

Parameters	Model A	Conventional
Maximum Torque [Nm]	0.4829	0.2048
Cogging Torque [Nm]	0.0076	0.0141
Iron Losses [W]	16.34	3.62
Torque Cogging Ratio	62	14
Torque Constant [Nm/A]	0.0386	0.016





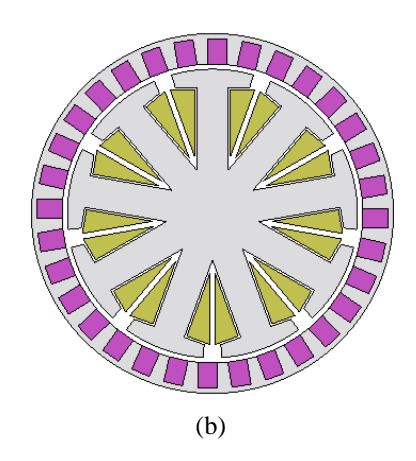


FIGURE 16 Structure of the (a) Proposed segmented stator (b) Salient pole stator

VI. CONCLUSION

This study conducts a comparative analysis of twelve distinct permanent magnet synchronous motor (PMSM) designs, categorized into four variations: width, tip angle, ratio, and skew angle. The JMAG Designer software package was employed to simulate and assess the performance of each proposed design. For the width and tip angle variations, the PM volume differed, whereas it remained constant in the other two variations. Key performance metrics, including generated torque, cogging torque, torque ratio, iron loss, and comparative analyses, were plotted for all PMSM models developed. Model A, demonstrating balanced and exceptional performance, was fabricated and subjected to experimental testing. The simulation and experimental results were validated within this study. Finally, Model A, featuring a segmented stator, was compared with a conventional PMSM structure. The key findings as below:

- I) In the width variation evaluation, Models A, B, and C were developed. Model A, with the smallest width, outperformed Model C (the largest width) by 6.48%, despite generating 4.18% less torque than Model B. Notably, Model A exhibited virtually no detent torque, in contrast to Models B and C, which produced detent torques 476.43% and 272.01% higher, respectively. Given its superior performance, Model A was designated the reference model.
- In the tip angle variation evaluation, Model K achieved generated torque comparable to Model A; however, its cogging torque was significantly higher at 221.09%.
- 3) Model P, sharing similar PMs volume with the reference model, exceeded Model A's performance by generating 44.56% greater torque.
- 4) The application of skew angle to the PM in the segmented stator yielded minimal differences, with Model A consistently producing higher torque despite identical PM volumes across models.

- 5) In terms of torque ratio, Model A delivered a highly favourable ratio, exceeding its cogging torque by a factor of 62. In comparison, Model B exhibited the lowest ratio at 11, while Model Q, the closest competitor, achieved a ratio of 25.
- 6) Radar graphs were utilized to depict the performance of all models, with Model A consistently forming a pentagonal shape indicative of balanced performance.
- 7) The fabricated Model A underwent experimental evaluation of torque-speed characteristics, static torque, and torque constant, demonstrating close alignment with simulation results.
- 8) Finally, Model A was compared with a conventional PMSM structure, both sharing identical parameters, particularly PM characteristics. The proposed motor with a segmented stator produced 135.79% higher generated torque, 45.22% lower detent torque, and a superior torque-to-cogging ratio. However, the conventional structure exhibited lower iron loss than Model A.



REFERENCES

- C. Liu, K. T. Chau, C. H. T. Lee, and Z. Song, "A Critical Review of Advanced Electric Machines and Control Strategies for Electric Vehicles," Jun. 01, 2021, *Institute of Electrical and Electronics* Engineers Inc. doi: 10.1109/JPROC.2020.3041417.
- [2] J. Wang, K. Atallah, Z. Q. Zhu, and D. Howe, "Modular three-phase permanent-magnet brushless machines for in-wheel applications," *IEEE Trans Veh Technol*, vol. 57, no. 5, pp. 2714–2720, 2008, doi: 10.1109/TVT.2007.914476.
- [3] C. H. T. Lee, W. Hua, T. Long, C. Jiang, and L. V. Iyer, "A Critical Review of Emerging Technologies for Electric and Hybrid Vehicles," 2021, Institute of Electrical and Electronics Engineers Inc. doi: 10.1109/OJVT.2021.3138894.
- [4] K. Dambrauskas, J. Vanagas, T. Zimnickas, A. Kalvaitis, and M. Ažubalis, "A method for efficiency determination of permanent magnet synchronous motor," *Energies (Basel)*, vol. 13, no. 4, 2020, doi: 10.3390/en13041004.
- [5] C. Sain, A. Banerjee, and P. K. Biswas, Control Strategies of Permanent Magnet Synchronous Motor Drive for Electric Vehicles. CRC Press, 2022. doi: 10.1201/9781003189558.
- [6] S. U. Chung, J. M. Kim, D. H. Koo, B. C. Woo, D. K. Hong, and J. Y. Lee, "Fractional slot concentrated winding permanent magnet synchronous machine with consequent pole rotor for low speed direct drive," *IEEE Trans Magn*, vol. 48, no. 11, pp. 2965– 2968, 2012, doi: 10.1109/TMAG.2012.2196417.
- [7] S. U. Chung, J. W. Kim, Y. Do Chun, B. C. Woo, and D. K. Hong, "Fractional slot concentrated winding PMSM with consequent pole rotor for a low-speed direct drive: Reduction of rare-earth permanent magnet," *IEEE Transactions on Energy Conversion*, vol. 30, no. 1, pp. 103–109, 2015, doi: 10.1109/TEC.2014.2352365.
- [8] S. U. Chung, S. H. Moon, D. J. Kim, and J. M. Kim, "Development of a 20-pole-24-slot SPMSM with consequent pole rotor for in-wheel direct drive," *IEEE Transactions on Industrial Electronics*, vol. 63, no. 1, pp. 302–309, Jan. 2016, doi: 10.1109/TIE.2015.2472375.
- [9] I. Petrov and J. Pyrhonen, "Performance of low-cost permanent magnet material in PM synchronous machines," *IEEE Transactions on Industrial Electronics*, vol. 60, no. 6, pp. 2131–2138, 2013, doi: 10.1109/TIE.2012.2191757.
- [10] V. I. Vlachou et al., "Overview on Permanent Magnet Motor Trends and Developments," Jan. 01, 2024, Multidisciplinary Digital Publishing Institute (MDPI). doi: 10.3390/en17020538.
- [11] M. E. Beniakar, P. E. Kakosimos, C. T. Krasopoulos, A. G. Sarigiannidis, and A. G. Kladas, "Comparison of In-wheel Permanent Magnet Motors for Electric Traction," in 2014 International Conference on Electrical Machines (ICEM), Berlin, Germany, 2014, pp. 2472–2478.
- [12] F. Li, K. Wang, J. Li, and H. Y. Sun, "Electromagnetic performance analysis of consequent-pole PM machine with asymmetric magnetic pole," *IEEE Trans Magn*, vol. 55, no. 6, Jun. 2019, doi: 10.1109/TMAG.2019.2904948.
- [13] L. Guo, Q. Li, and H. Wang, "Design and analysis of consequent pole permanent magnet synchronous motor with low torque ripple," *IET Electr Power Appl*, vol. 17, no. 4, pp. 547–561, Apr. 2023, doi: 10.1049/elp2.12284.
- [14] Miguel Esteban Romero, "Analysis and Comparison of the Interior Permanent Magnet Motor Design with Different Magnetic Materials," in 2020 IEEE International Conference on Electro Information Technology (EIT), Chicago, IL, USA: IEEE, Sep. 2020.
- [15] Kan Akatsu, Katsuyuki Narita, Yoshiyuki Sakashita, and Takashi Yamada, "Characteristics comparison between SPMSM and IPMSM under high flux density condition by both experimental and analysis results," in 2008 International Conference on Electrical Machines and Systems, 2008.
- [16] Z. Q. Zhu, Z. P. Xia, Y. F. Shi, D. Howe, A. Pride, and X. J. Chen, "Performance of Halbach Magnetized Brushless AC Motors," *IEEE Trans Magn*, vol. 39, no. 5 II, pp. 2992–2994, 2003, doi: 10.1109/TMAG.2003.816717.
- [17] S. Kumawat, S. Bhaktha, and K. V. Gangadharan, "Enhancing Torque performance with Dual Teeth Switched Reluctance Motor:

8

- A Novel Approach," in 2021 IEEE International Power and Renewable Energy Conference, IPRECON 2021, Institute of Electrical and Electronics Engineers Inc., 2021. doi: 10.1109/IPRECON52453.2021.9640842.
- [18] Ehsan Farmahini Farahani, Mohammad Amin Jalali Kondelaji, and Mojtaba Mirsalim, "Divided Teeth Switched Reluctance Motor with Different Tooth Combinations," 2020 11th Power Electronics, Drive Systems, and Technologies Conference (PEDSTC)., 2020.
- [19] C. Liu, K. T. Chau, C. H. T. Lee, F. Lin, F. Li, and T. W. Ching, "Magnetic vibration analysis of a new DC-excited multitoothed Switched reluctance machine," *IEEE Trans Magn*, vol. 50, no. 11, Nov. 2014, doi: 10.1109/TMAG.2014.2323706.
- [20] H. F. Hairulnizam, N. Misron, N. A. Ibrahim, E. Muhammad, and C. A. Vaithilingam, "Performance Analysis of Stator Structure in Divided Teeth Outer Rotor Embedded Permanent Magnet Synchronous Motor: Salient Pole Stator vs Segmented Stator," Progress In Electromagnetics Research C, vol. 146, pp. 141–150, 2024, doi: 10.2528/PIERC24040904.
- [21] Yasuo Oshinoya, Electrical Machine. Kyoritsu Publishing Co., Ltd, 2005.





HAIRUL FAIZI HAIRULNIZAM was born in Seremban, Negeri Sembilan, Malaysia. He obtained his bachelor's degree in electrical and Electronics Engineering from Universiti Putra Malaysia in 2023. Currently pursuing his Master which he dedicated to innovating permanent magnet synchronous motor technology, with a keen interest in enhancing motor performance and application versatility.



HAFIZ RASHIDI RAMLI (Member, IEEE) received the B.Eng. degree in electrical and electronic engineering and the M.Sc. degree in control and automation engineering from Universiti Putra Malaysia (UPM), in 2007 and 2010, respectively, and the Ph.D. degree in biomedical engineering from Imperial College London, in 2017. Currently, he is a Professional Engineer and a Senior Lecturer with UPM, where his research interests include artificial intelligence, computer vision, robotics, and haptics.



NORHISAM MISRON (Member, IEEE) received the B.Eng., M.Eng., and Dr.Eng. degrees in System Engineering from Shinshu University, Nagano, Japan, in 1998, 2000, and 2003, respectively. He joined the Department of Electrical and Electronic Engineering at Universiti Putra Malaysia as a Lecturer in 2003, advancing to Associate Professor in 2009 and Full Professor in 2016. He is also an Associate Researcher with the Institute of Advanced Technology (ITMA) and the Institute of Plantation Studies (IPS). His research interests

encompass magnetic applications, particularly in sensor and electrical machine development. His current work focuses on designing and developing sensor and actuator technologies for the oil palm industry as well as motor and generator for clean energy. He actively serves on various IEEE technical committees.



CHOCKALINGAM ARAVIND VAITHILINGAM (Senior Member, IEEE) Dr. Chockalingam Aravind Vaithilingam earn his PhD in 2013 currently the Director for the Clean Technology Impact Lab at Taylor's University Malaysia. His research work is aligned with the sustainable developmental goals on clean water sanitation (SDG6) and affordable and clean energy (SDG7).



8

NUR AMIRA IBRAHIM received the Bachelor of Engineering degree in electrical and electronics from Universiti Putra Malaysia, Malaysia, in 2020, where she is currently pursuing the PhD. with the Faculty of Engineering. Her current research interest includes the development of generator for vertical axis wind turbine.